BRAIN
ORIGINAL ARTICLE

Brain atrophy in prodromal synucleinopathy is shaped by structural connectivity and gene expression

Shady Rahayel,[1,2] Christina Tremblay,[1] Andrew Vo,[1] Ying-Qiu Zheng,[3] Stéphane Lehéricy,[4] Isabelle Arnulf,[4] Marie Vidailhet,[4] Jean-Christophe Corvol,[4] ICEBERG Study Group[4] Jean-François Gagnon,[2,5,6] Ronald B. Postuma,[2,7] Jacques Montplaisir,[2,8] Simon Lewis,[9] Elie Matar,[9] Kaylena Ehgoetz Martens,[9,10] Per Borghammer,[11] Karoline Knudsen,[11] Allan Hansen,[11] Oury Monchi,[6,12] Bratislav Misic[1,†] and Alain Dagher[1,†]

[†]These authors contributed equally to this work.

See Arnaldi and Mattioli (https://doi.org/10.1093/brain/awac242) for a scientific commentary on this article.

Isolated REM sleep behaviour disorder (iRBD) is a synucleinopathy characterized by abnormal behaviours and vocalizations during REM sleep. Most iRBD patients develop dementia with Lewy bodies, Parkinson's disease or multiple system atrophy over time. Patients with iRBD exhibit brain atrophy patterns that are reminiscent of those observed in overt synucleinopathies. However, the mechanisms linking brain atrophy to the underlying alpha-synuclein pathophysiology are poorly understood. Our objective was to investigate how the prion-like and regional vulnerability hypotheses of alpha-synuclein might explain brain atrophy in iRBD.

Using a multicentric cohort of 182 polysomnography-confirmed iRBD patients who underwent T_1-weighted MRI, we performed vertex-based cortical surface and deformation-based morphometry analyses to quantify brain atrophy in patients (67.8 years, 84% male) and 261 healthy controls (66.2 years, 75%) and investigated the morphological correlates of motor and cognitive functioning in iRBD. Next, we applied the agent-based Susceptible–Infected–Removed model (i.e. a computational model that simulates *in silico* the spread of pathologic alpha-synuclein based on structural connectivity and gene expression) and tested if it recreated atrophy in iRBD by statistically comparing simulated regional brain atrophy to the atrophy observed in patients. The impact of *SNCA* and *GBA* gene expression and brain connectivity was then evaluated by comparing the model fit to the one obtained in null models where either gene expression or connectivity was randomized.

The results showed that iRBD patients present with cortical thinning and tissue deformation, which correlated with motor and cognitive functioning. Next, we found that the computational model recreated cortical thinning ($r = 0.51$, $P = 0.0007$) and tissue deformation ($r = 0.52$, $P = 0.0005$) in patients, and that the connectome's architecture along with *SNCA* and *GBA* gene expression contributed to shaping atrophy in iRBD. We further demonstrated that the full agent-based model performed better than network measures or gene expression alone in recreating the atrophy pattern in iRBD.

In summary, atrophy in iRBD is extensive, correlates with motor and cognitive function and can be recreated using the dynamics of agent-based modelling, structural connectivity and gene expression. These findings support the concepts that both prion-like spread and regional susceptibility account for the atrophy observed in prodromal synucleinopathies. Therefore, the agent-based Susceptible–Infected–Removed model may be a useful tool for testing hypotheses underlying neurodegenerative diseases and new therapies aimed at slowing or stopping the spread of alpha-synuclein pathology.

1 The Neuro (Montreal Neurological Institute-Hospital), McGill University, Montreal H3A 2B4, Canada
2 Centre for Advanced Research in Sleep Medicine, Hôpital du Sacré-Cœur de Montréal, Montreal H4J 1C5, Canada

Received December 23, 2021. Revised May 06, 2022. Accepted May 12, 2022. Advance access publication May 20, 2022

3 Wellcome Centre for Integrative Neuroimaging, Centre for Functional Magnetic Resonance Imaging of the Brain, University of Oxford, John Radcliffe Hospital, Oxford OX3 9DU, UK
4 Sorbonne Université, Institut du Cerveau—Paris Brain Institute—ICM, INSERM, CNRS, Assistance Publique Hôpitaux de Paris, Pitié-Salpêtrière Hospital, Paris 75013, France
5 Department of Psychology, Université du Québec à Montréal, Montreal H2X 3P2, Canada
6 Research Centre, Institut universitaire de gériatrie de Montréal, Montreal H3W 1W5, Canada
7 Department of Neurology, Montreal General Hospital, Montreal H3G 1A4, Canada
8 Department of Psychiatry, Université de Montréal, Montreal H3T 1J4, Canada
9 ForeFront Parkinson's Disease Research Clinic, Brain and Mind Centre, University of Sydney, Camperdown, NSW 2050, Australia
10 Department of Kinesiology and Health Sciences, University of Waterloo, Waterloo N2L 3G1, Canada
11 Department of Nuclear Medicine and PET, Aarhus University Hospital, Aarhus DK-8200, Denmark
12 Departments of Clinical Neurosciences, Radiology, and Hotchkiss Brain Institute, University of Calgary, Calgary T2N 4N1, Canada

Correspondence to: Shady Rahayel, PhD
The Neuro (Montreal Neurological Institute-Hospital)
McGill University, 3801 University Street
Montreal, Quebec, Canada, H3A 2B4
E-mail: shady.rahayel@mcgill.ca

Keywords: REM sleep behaviour disorder; Parkinson's disease; dementia with Lewy bodies; alpha-synuclein; MRI

Abbreviations: DBM = deformation-based morphometry; iRBD = isolated REM sleep behaviour disorder; MDS-UPDRS-III = Movement Disorders Society–Unified Parkinson's Disease Rating Scale, motor examination MoCA = Montreal Cognitive Assessment; SIR = Susceptible–Infected–Removed

Introduction

Isolated REM sleep behaviour disorder (iRBD) is characterized by abnormal motor behaviours and vocalizations during REM sleep.[1,2] iRBD typically develops into dementia with Lewy bodies, Parkinson's disease or multiple system atrophy,[3,4] making it an early manifestation and phenotype of synucleinopathies. Specifically, iRBD is thought to result from the impairment of brainstem circuits involved in REM sleep muscle atonia that occurs as a result of early accumulation of pathologic alpha-synuclein in the pontine tegmentum.[5,6] However, MRI studies in patients with polysomnography-proven iRBD without cognitive or motor diagnoses have also shown patterns of diffuse brain atrophy reminiscent of dementia with Lewy bodies or Parkinson's disease.[7,8] Moreover, the severity of cortical atrophy is a predictor of subsequent dementia, hence more severe disease.[9]

Dementia with Lewy bodies and Parkinson's disease are thought to arise from the propagation and accumulation of misfolded alpha-synuclein in the brain.[10] There may be different routes of propagation, accounting for different syndromes.[11] Braak *et al.*[12,13] hypothesized that one of the most common pathways would start in the lower brainstem and spread upward to the midbrain and cerebral hemispheres, giving rise to iRBD followed by phenoconversion to Parkinson's disease or dementia with Lewy bodies. Evidence from animal models shows that pathological alpha-synuclein can propagate and promote protein misfolding, supporting the prion-like model of alpha-synuclein.[5,14–19] In line with this, MRI studies performed in patients with Parkinson's disease also show that brain atrophy patterns are shaped by brain connectivity.[20–22]

We previously modelled alpha-synuclein propagation using a Susceptible–Infected–Removed (SIR) agent-based model,[23] a computational model based on an adaptation of epidemiological SIR models but applied to neurological diseases with the underlying hypothesis that alpha-synuclein propagation works like an infection in a population. In this model, the agents are autonomous alpha-synuclein molecules that can exist in three states: Susceptible (normal), Infected (misfolded) or Removed (degraded). In its misfolded state, the agent becomes pathological. Agents can also move between regions via neural connections. The model uses *SNCA* and *GBA* gene expression as measures of local alpha-synuclein concentration and connectivity to determine agent numbers and propagation. In this model, *SNCA* expression determines alpha-synuclein production and *GBA* expression influences degradation of both normal and misfolded alpha-synuclein. The model has predicted atrophy distribution in Parkinson's disease patients and pathological alpha-synuclein distribution in a mouse model.[23,24] Null models show that both connectivity and local alpha-synuclein concentration are important factors shaping the propagation of agents.[23,24] However, it remains unknown if these mechanisms also explain the atrophy seen in prodromal synucleinopathies.

In this study, we compiled neuroimaging data from several centres to generate a map of brain atrophy in iRBD. We then used the agent-based SIR model to test if brain connectivity and *SNCA* and *GBA* gene expression explain brain atrophy patterns in iRBD. Vertex-based cortical surface and deformation-based morphometry (DBM) analyses were performed in 182 polysomnography-confirmed iRBD patients and 261 healthy controls who underwent T_1-weighted brain MRI to characterize atrophy and investigate the correlates of motor and cognitive functioning. We then tested whether the SIR model using brain connectivity and gene expression could recreate the actual atrophy pattern found in iRBD. We used null modelling to test whether connectivity and gene expression were decisive in shaping the brain atrophy seen in iRBD. We hypothesized that the SIR model would recreate brain atrophy in iRBD and that both connectivity

and *SNCA* and *GBA* gene expression would be significant determinants of atrophy.

Materials and methods

Participants

A total of 443 participants (182 iRBD patients and 261 controls) were recruited from five sites: 116 (59 patients) from the Movement Disorders clinic at the Hôpital de la Pitié-Salpêtrière (France, Appendix 1), 83 (48 patients) from the Centre for Advanced Research on Sleep Medicine at the Hôpital du Sacré-Cœur de Montréal (Canada), 56 (30 patients) from the ForeFront Parkinson's Disease Research Clinic at the University of Sydney (Australia), 38 (18 patients) from Aarhus University Hospital (Denmark) and 150 (27 patients) from the Parkinson's Progression Markers Initiative baseline cohort.[25] All iRBD patients had a polysomnography-confirmed diagnosis of iRBD and were free of parkinsonism and dementia at the clinical examination closest in time to MRI.[26,27] Patients underwent the Unified Parkinson's Disease Rating Scale, part III (UPDRS-III) and the Montreal Cognitive Assessment (MoCA) to assess motor and cognitive functions, respectively. An overview of the study protocol along with a flowchart of the selected patients is presented in Fig. 1 and the cohorts' demographics are available in Supplementary Table 1. All participants were part of research protocols approved by local ethics committees and provided written informed consent according to the Declaration of Helsinki. The current project was also approved by the Research Ethics Board of the McGill University Health Centre.

MRI

MRI acquisition

The Montreal cohort underwent T_1-weighted imaging with a 3 T Siemens TIM Trio scanner with a 12-channel head coil, MPRAGE sequence: repetition time (TR): 2300 ms, echo time (TE): 2.91 ms, flip angle: 9° and voxel size: 1 mm³ isotropic. The Paris cohort underwent T_1-weighted imaging with a 3 T Siemens TIM Trio scanner with a 12-channel head coil, MPRAGE sequence: TR: 2300 ms, TE: 4.18 ms, inversion time (TI): 900 ms, flip angle: 9° and voxel size: 1 mm³ isotropic; or a 3 T PRISMA Fit scanner with a 64-channel head coil, MP2RAGE sequence: TR: 5000 ms, TE: 2.98 ms, TI: 700 and 2500 ms, flip angle: 4° and 5°, GRAPPA: 3 and voxel size: 1 mm³ isotropic. The Sydney cohort was imaged with a GE Discovery MR750 3 T scanner with an 8-channel head coil, BRAVO sequence: TR: 5800 ms, TE: 2.6 ms, flip angle: 12° and voxel size: 1 mm³ isotropic. The Aarhus cohort was imaged with a 3 T Siemens MAGNETOM Skyra scanner with a 32-channel head coil, MPRAGE sequence: TR: 2420 ms, TE: 3.7 ms, TI: 960 ms, flip angle: 9° and voxel size: 1 mm³ isotropic. The T_1-weighted images from the Parkinson's Progression Markers Initiative cohort, an international multicentre cohort, were also included (see www.ppmi-info.org for the imaging protocols).[25]

Quantification of atrophy

DBM was performed using CAT12 (version 12.7; www.neuro.uni-jena.de/cat) to quantify atrophy by measuring the non-linear change required in every voxel to register the brain to the common template (IXI555 MNI152 template).[28] The processing included bias correction, affine registration, unified segmentation,[29] skull-stripping, parcellation, intensity transformation, partial volume estimation and spatial normalization using DARTEL.[30] This resulted in whole-brain maps of Jacobian determinants, which were smoothed with a 12 mm isotropic kernel and then used as the measure of local brain atrophy. Images with an automated quality rating below 80% were excluded from analyses involving DBM.

Brain atrophy in iRBD also manifests as abnormal cortical thickness and surface area.[31] To ensure that findings were not due to the atrophy metric, the scans passing DBM quality control were also processed with FreeSurfer (version 6.0.0) to generate individual thickness and surface area maps of the whole cortex.[32,33] Every map was inspected by a trained rater (S.R.) and a score from 1 to 4 was assigned to each scan based on published guidelines[34,35]; scans with a score >2 (i.e. major reconstruction errors) were excluded from cortical surface analyses.

W-scoring and brain parcellation

To test the computational model, observed atrophy was corrected for the effects of age, sex and site using a W-scoring procedure.[36,37] For DBM-derived atrophy, a W-score map was computed from each patient's smoothed map by regressing out the effects of age, sex and site found in the age- and sex-matched controls passing quality control.[36] At each voxel, the following formula was applied:

$$\text{Wscore} = \frac{\left(\begin{array}{c}\text{iRBD raw value} - \text{control value expected} \\ \textit{for the patient's} \text{ age, sex, and site}\end{array}\right)}{\text{SD of the residuals in controls}} \quad (1)$$

A voxel with a negative W-score represents decreased volume in the iRBD patient compared to controls, whereas a positive W-score indicates increased volume, while considering the confounds.

Regional W-scores were then extracted by parcellating every map with a 42-region atlas for which corresponding structural connectivity and gene expression data were available.[23] This atlas comprised 34 cortical regions from the Desikan–Killiany atlas and seven subcortical regions from FreeSurfer.[38,39] Due to its importance in synucleinopathies,[40,41] the substantia nigra was added from the 7-T 'Atlas of the basal ganglia' (ATAG atlas).[42] The 42 regional W-scores extracted from each map were then averaged across iRBD patients to yield 42 W-scores representing regional tissue deformation. W-scores were also extracted using finer parcellations of 65 and 119 regions to ensure that findings were robust to parcellation resolution. The main analyses were performed in the left hemisphere because gene expression data, used by the model for determining regional alpha-synuclein synthesis and clearance (see below), were available for all six left hemispheres but only two of the right hemispheres from the post-mortem brains,[43] and because diffusion tractography-based reconstruction of the connectome is inaccurate for interhemispheric connections.[44,45]

For cortical surface analysis, thickness and surface area values were extracted from each of the 34 atlas regions used for the DBM analysis above.[38] As subcortical regions do not have a cortical surface from which to derive thickness and area values, the global volume measurement generated as part of FreeSurfer's subcortical processing was used. The substantia nigra was excluded from cortical surface analyses as it is unavailable in FreeSurfer, resulting in a total of 41 regions. As cortical surface area and subcortical volume scale with head size,[46,47] the raw values were divided by the estimated total intracranial volume (derived from FreeSurfer). The same W-scoring procedure was then applied to these values to adjust for the effects of age, sex and site from controls who passed quality control. To ascertain those findings were not due to the multicentric nature of the cohort, we also tested the model with

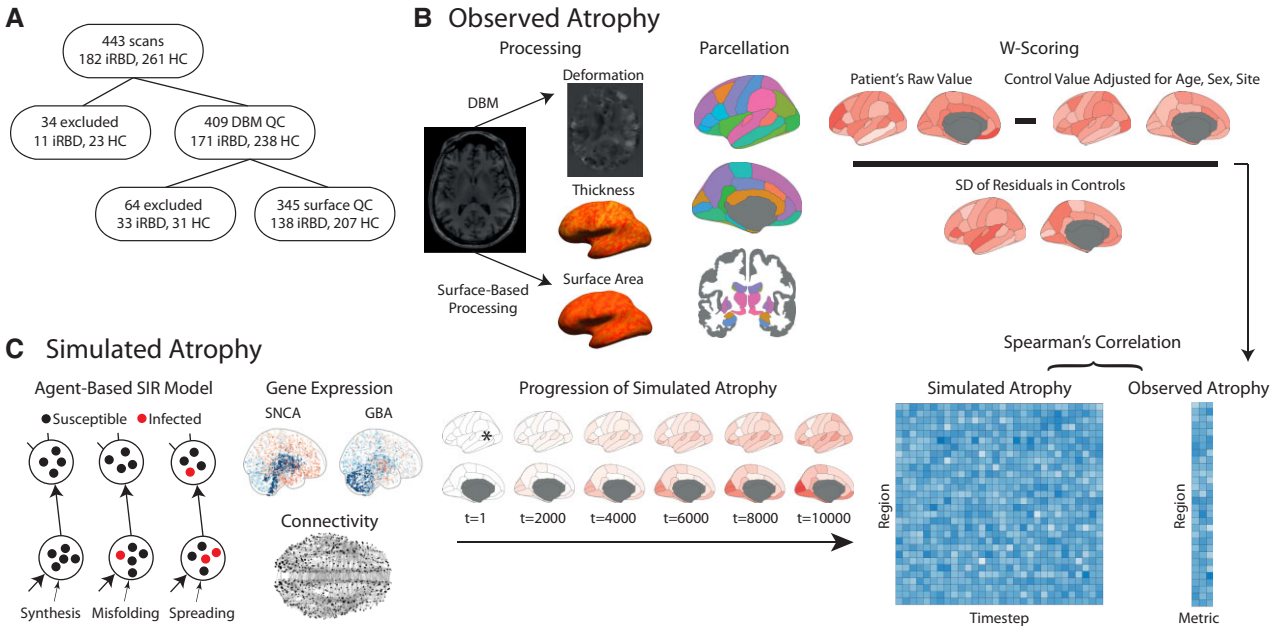

Figure 1 Demographics and clinical variables of iRBD and controls. (**A**) A flow chart of the different cohorts included in this study. (**B**) Overview of the study protocol for quantifying brain atrophy in iRBD. DBM and surface-based cortical processing were performed to generate Jacobian and cortical thickness and surface maps. These were parcellated and W-scored to correct for the effects of age, sex and site seen in controls. These regional values were the atrophy patterns to recreate. (**C**) The spread of alpha-synuclein in the brain was simulated *in silico* using the agent-based SIR model based on structural connectomics and *SNCA* and *GBA* gene expression. The simulation was iterated 10 000 times, with brain atrophy being simulated at each time step. These patterns were correlated with the observed atrophy patterns to assess if the model recreated atrophy. HC = healthy controls; QC = quality control.

harmonized regional W-scores derived from the ComBat harmonization method,[48–50] a batch-effect correction tool used in genomics and validated for neuroimaging that removes the unwanted scanning-related intersite variability while preserving biological variability.

Importantly, to facilitate interpretation when testing the model, the W-scores were inverted such that a positive score indicated a region with decreased volume and a negative score indicated increased volume in iRBD patients compared to controls.

Agent-based SIR model

Model overview

The agent-based SIR model (https://github.com/yingqiuz/SIR_simulator) was used to simulate the spread of alpha-synuclein.[23] This algorithm applies agent-based modelling within a SIR framework to model the distribution of pathologic alpha-synuclein as an epidemic shaped by the simultaneous effect of brain connectivity and *SNCA* and *GBA* expression.[23] This model previously recreated the atrophy observed in Parkinson's disease and, using *MAPT*, *GRN*, *C9orf72* and *TARDBP* instead of *SNCA* and *GBA*, the atrophy observed in the behavioural variant of frontotemporal dementia.[23,51] In this model, every agent is an autonomous alpha-synuclein molecule that belongs to one of three mutually exclusive states: the 'Susceptible' state when the agent is normal (normal alpha-synuclein), the 'Infected' state when the agent becomes pathologic (misfolded alpha-synuclein isoform) and the 'Removed' state when the agent is degraded. Agents can also move between regions via neural connections. The transitions between states are determined by rules guiding the interaction dynamics between agents and their regional environment. The model simulates atrophy in every brain region based on the following computational steps: (i) the production of normal alpha-synuclein; (ii) the clearance of normal and misfolded alpha-synuclein; (iii) the misfolding of normal alpha-synuclein; (iv) the propagation of normal and misfolded alpha-synuclein; and (v) the emergence of atrophy.

Connectivity and gene data

The connectome used to model the spread of agents from one region to another was derived from a separate group of young healthy individuals. The details of diffusion-weighted image processing, deterministic fibre tracking and gene expression data have been described elsewhere.[23] Briefly, the structural connectivity data were derived from the preprocessed diffusion-weighted images of 1027 participants from the Human Connectome Project.[52] Deterministic tractography was used to construct consensus connectivity matrices between the 42 regions as described previously.[53–55] The analysis was performed at connection densities of 25%, 30%, 35% and 40% to ensure that results were robust to change in this parameter. A distance matrix of the mean Euclidean length of the corresponding streamlines for the 42 regions was also generated to modulate the rate of movement of agents between connected regions.

For the gene expression data, the regional expression of *SNCA* and *GBA* were used to model the regional synthesis and clearance of alpha-synuclein; values were derived from the post-mortem mRNA transcription profiles of six subjects from the Allen Human Brain Atlas[43] using *abagen* (https://abagen.readthedocs.io/en/stable/).[56] The Allen Human Brain Atlas is a comprehensive gene expression atlas of the adult human brain based on 3702 cortical and subcortical tissue samples in which the transcription profiles of more than 20 000 genes were measured. Due to its whole-brain spatial coverage, it can be used to extract regional gene expression values in user-defined parcellations.[57] Here, the *SNCA* and *GBA* transcription profiles of the six brains were averaged for the 42 left-hemisphere regions of the parcellation to yield *SNCA* and *GBA* expression vectors that were used for the model.

Production of normal alpha-synuclein: module 1

In region i, the synthesis of susceptible agents per unit time occurs with probability α_i:

$$\alpha_i = \mathbf{\Phi}_{0,1}(\text{SNCAexpression}_i) \quad (2)$$

where $\Phi_{0,1}(\cdot)$ is the standard normal cumulative distribution function and SNCAexpression_i is the gene expression of *SNCA* of region *i*. At each time step, the increment of susceptible agents in region *i* is $\alpha_i S_i \Delta t$, where S_i is the size of region *i* and Δt is the total time.

Clearance of normal and misfolded alpha-synuclein: module 2

In region i, the clearance of susceptible and infected agents per unit time occurs with probability β_i:

$$\beta_i = \mathbf{\Phi}_{0,1}(\text{GBAexpression}_i) \quad (3)$$

where GBAexpression_i is the gene expression of *GBA* of region *i*. Considering that the probability that an agent is still active after Δt is given by $\lim_{\delta\tau\to 0}(1-\beta\delta\tau)^{\Delta t/\delta\tau} = e^{-\beta\Delta t}$, the cleared proportion within Δt is $1-e^{-\beta\Delta t}$.

Misfolding of normal alpha-synuclein: module 3

The susceptible agents not cleared from region *i* may become infected per unit time with probability γ_i:

$$\gamma_i = 1 - e^{M_i \ln(1-\gamma_i^0)} \quad (4)$$

where M_i is the population of infected agents in region *i* and γ_i^0 is the baseline likelihood that a susceptible agent becomes an infected agent in region *i*, which was set as the reciprocal of region size. The probability that a susceptible agent did not get infected is given by $(1-\gamma_i^0)^{M_i}$; therefore, $\gamma_i = 1-(1-\gamma_i^0)^{M_i} = 1 - e^{M_i \ln(1-\gamma_i^0)}$ represents the probability that a susceptible agent becomes infected in region *i* per unit time. Similarly, the probability that an agent is still susceptible after Δt is given by $\lim_{\delta\tau\to 0}(1-\gamma_i^0\delta\tau)^{M_i\Delta t/\delta\tau} = e^{-\gamma_i^0 M_i \Delta t}$, with the proportion of agents becoming infected after Δt being $1-e^{-\gamma_i^0 M_i \Delta t}$.

To determine the baseline density of susceptible agents in every region, the population of susceptible agents N_i is incremented with:

$$\Delta N_i = \alpha_i S_i \Delta t - (1-e^{-\beta_i \Delta t}) N_i \quad (5)$$

Once the system reaches its stable point (error tolerance $\epsilon < 10^{-7}$), the pathogenic spread and update of N_i and M_i is given by:

$$\Delta N_i = \alpha_i S_i \Delta t - (1-e^{-\beta_i \Delta t}) N_i - (e^{-\beta_i \Delta t})(1-e^{-\gamma_i^0 M_i \Delta t}) N_i \quad (6)$$

$$\Delta M_i = (e^{-\beta_i \Delta t})(1-e^{-\gamma_i^0 M_i \Delta t}) N_i - (1-e^{-\beta_i \Delta t}) M_i \quad (7)$$

Propagation of normal and misfolded alpha-synuclein: module 4

Susceptible and infected agents in region *i* either remain in region *i* or spread to other regions based on a multinomial distribution per unit time with probabilities:

$$P_{region_i \to region_i} = \rho_i \quad (8)$$

$$P_{region_i \to edge_{ij}} = (1-\rho_i)\frac{w_{ij}}{\sum_j w_{ij}} \quad (9)$$

where w_{ij} is the connection strength between regions *i* and *j* and ρ_i is the probability that an agent remains in region *i*. The main analyses were performed using $\rho = 0.5$ for all regions, but ρ values from 0.1 to 0.9 were also tested to ensure that findings did not depend solely on this parameter.

The susceptible and infected agents located inside an edge could exit the edge per unit time based on binary probabilities:

$$P_{edge_{ij} \to region_j} = \frac{1}{l_{ij}} \quad (10)$$

$$P_{edge_{ij} \to edge_{ij}} = 1 - \frac{1}{l_{ij}} \quad (11)$$

where l_{ij} is the length of the edge between regions *i* and *j*. The increment in N_i and M_i in region *i* after total time Δt is given by:

$$\Delta N_i = \sum_j \frac{1}{l_{ji}} N_{ji} \Delta t - (1-\rho_i) N_i \Delta t \quad (12)$$

$$\Delta M_i = \sum_j \frac{1}{l_{ji}} M_{ji} \Delta t - (1-\rho_i) M_i \Delta t \quad (13)$$

whereas the increment in the population of susceptible and infected agents inside the edge between regions *i* and *j* (N_{ij} and M_{ij}, respectively) after total time Δt is:

$$\Delta N_{ij} = (1-\rho_i)\frac{w_{ij}}{\sum_j w_{ij}} N_i \Delta t - \frac{1}{l_{ij}} N_{ij} \Delta t \quad (14)$$

$$\Delta M_{ij} = (1-\rho_i)\frac{w_{ij}}{\sum_j w_{ij}} M_i \Delta t - \frac{1}{l_{ij}} M_{ij} \Delta t \quad (15)$$

Emergence of simulated atrophy: module 5

Regional atrophy was simulated as the sum of two processes: the direct toxicity resulting from the regional accumulation of infected agents and the deafferentation caused by cell death in connected regions. In region *i*, the atrophy accrual is given by:

$$\Delta L_i(t) = k_1(1-e^{-r_i(t)\Delta t}) + k_2 \sum_j \frac{w_{ji}}{\sum_j w_{ji}}(1-e^{-r_j(t-1)\Delta t}) \quad (16)$$

where $r_i(t)$ is the proportion of infected agents in region *i* at time *t* and $1-e^{-r_i(t)\Delta t}$ is the increment of atrophy at time *t* caused by the accumulation of alpha-synuclein pathology within Δt. The first term controls the direct impact of infected agents, whereas the second term weighs the increment of atrophy based on deafferentation from neighbouring regions. Each term was given a weight k_1 and k_2 of 0.5 for the main analyses, but weights varying from 0.1 to 0.9 were also tested to ensure that findings were not due to this parameter only. In other words, this module generated, at every time step, a value of simulated atrophy for each of the 42 regions; it is this simulated atrophy that was correlated with the observed atrophy to test if the model accurately recreated the brain atrophy of iRBD.

Statistical analysis

Between group differences in atrophy

To investigate the presence of structural differences between groups, we performed brain-wide comparisons between iRBD

patients and controls, with age, sex and site entered as covariates in the models. For DBM-derived tissue deformation, two-tailed general linear models with age, sex and site as covariates were performed to investigate the presence of significant differences between iRBD patients and controls. The Benjamini–Hochberg procedure was used to correct for the rate of false discoveries at a statistical threshold of $P < 0.05$.[58]

For surface-based cortical measurements, general linear models were performed at each vertex to investigate the presence of significant differences in cortical thickness or surface area in iRBD patients compared to controls. Surface maps were smoothed using a 15 mm full-width, half-maximum kernel and age, sex and site were entered as covariates, as well as estimated total intracranial volume for surface area. The surface correlates of motor and cognitive functioning in iRBD were also investigated in participants with available Movement Disorders Society (MDS)-UPDRS-III (90 patients, 130 controls) or MoCA (134 patients, 174 controls) scores. Using age, sex and site (and total intracranial volume for cortical surface area) as covariates, vertex-based analyses were performed to investigate the vertices significantly correlated with clinical variables. Another contrast matrix was also created to identify the vertices where thickness and surface area correlations with the MDS-UPDRS-III or MoCA scores differed significantly between iRBD patients and controls. Statistical significance was determined by Monte Carlo simulation at a corrected threshold of $P < 0.05$.

Replication of observed atrophy

To assess if the SIR model recreated atrophy, the spread of pathological alpha-synuclein was simulated *in silico* by injecting pathology in one region, simulating the propagation over 10 000 time steps and repeating the process for every region as seed. At each time step, the model generated regional values representing the amount of simulated atrophy and the simulated number of infected and susceptible agents. To avoid interpreting any spurious overfit of the model when assessing the fit between atrophy patterns, because some regions may act as outliers due to agents being present in only a few brain regions when initiating the spread, we discarded all the time steps where the number of infected agents in any region increased by more than 1% compared to the previous time step.

At each time step, Spearman's rank correlations were used to assess the positive association between simulated atrophy and observed atrophy in patients. The highest correlation coefficient, if statistically significant at $P < 0.0012$ (Bonferroni-corrected threshold for the 42 regions), was considered as the peak fit. As thickness *W*-scores correlated with region size ($r = 0.54$, $P = 0.0013$), the scores were divided by the region size before assessing the peak fit. For cortical surface measurements, the peak fit was also assessed over the 34 cortical regions only to ensure that the peak fit was not driven mostly by subcortical regions. In addition, to investigate if the atrophy simulated by the SIR model was associated with clinical features, we measured the peak fits obtained between the atrophy pattern simulated by the model and the atrophy pattern observed in each patient separately. These individual peak fits were then entered into partial correlations with age and sex as covariates to investigate if the association between a patient's atrophy pattern and the one simulated by the model correlated significantly with MoCA and MDS-UPDRS-III scores. The *ggseg* package was used for visualization.[59]

Assessment of other clearance genes

To explore whether genes other than *GBA* may influence alpha-synuclein metabolism in the model, we assessed the peak fits obtained when using the expression of genes involved in the autophagy lysosomal pathway. We used the Molecular Signatures Database (version 7.5.1, http://www.gsea-msigdb.org/gsea/msigdb/index.jsp) to identify genes related to this pathway and tested separately the 310 genes belonging to the Gene Ontology Consortium macroautophagy biological process gene set (accession ID: GO:0016236),[60] which includes several genes known for their involvement in the development of Parkinson's disease and dementia with Lewy bodies such as *LRRK2*, *ATP13A2*, *VPS35*, *PINK1* and *PRKN*.[61] Brain expression values for each of the genes were extracted from the Allen Human Brain Atlas for the 42-region atlas using *abagen* and the SIR model was re-run at each connection density with each gene expression value entered separately as the clearance term, replacing *GBA* in the original model.

For visualization purposes, the average gene expression across brain regions and cell types in the genes that led to the highest peak fits between simulated and observed atrophy patterns was extracted using Cytosplore Viewer (https://viewer.cytosplore.org/)[62–64] based on the Human Multiple Cortical Areas SMART-Seq database from the Allen Brain Atlas (https://portal.brain-map.org/atlases-and-data/rnaseq/human-multiple-cortical-areas-smart-seq). This brain cell database comprises single-nucleus transcriptomes of 49 495 nuclei from post-mortem and neurosurgical human brain tissues dissected from the middle temporal gyrus, anterior cingulate gyrus, primary visual cortex, primary motor cortex, primary somatosensory cortex and primary auditory cortex. Nuclei were previously grouped into transcriptomic cell types based on an iterative clustering procedure[65] that resulted in gene expression being measured, for GABAergic cells, in the *ADARB2*-expressing (caudal ganglionic eminence) branch (subdivided into *VIP* and *LAMP5 PAX6* cellular subclasses) and the *LHX6*-expressing (medial ganglionic eminence) branch (subdivided into *PVALB* and the *SST* subclasses); for glutamatergic cells, in the cells from the superficial and deep layers, the latter divided into *FEZF2*- and *RORB-/THEMIS*-expressing subclasses; and for non-neuronal cells, in astrocytes and oligodendrocytes/oligodendrocyte precursor cells.

Comparison with other model-derived, topological and gene metrics

To determine the influence of connectomics or regional vulnerability on the atrophy patterns of iRBD, we tested whether simpler measures predicted brain atrophy as well as the complete agent-based model. These measures included (i) model-derived measurements representing the number of infected and susceptible agents at each time step in each region; (ii) network measures alone, namely node degree, node strength, node betweenness centrality and eigenvector centrality, derived from the Brain Connectivity Toolbox (www.sites.google.com/site/bctnet/)[66]; (iii) *SNCA* and *GBA* regional expression alone. Node degree represents the number of edges (structural connections) connected to a node (region). Node strength represents the sum of the weights of the edges connected to the node. Node betweenness centrality represents the number of times a given node is found in the shortest paths linking every node pair in the network. Eigenvector centrality is a self-referential measure of centrality; nodes with high eigenvector centrality are connected with other nodes that also have high eigenvector centrality. Node betweenness centrality and eigenvector centrality identify hub regions.

Randomized null models

To test if brain connectivity and gene expression shaped the atrophy in iRBD, all fits between simulated and measured atrophy patterns were tested against null models in which network topology and geometry or gene expression was randomized. For the

connectome, rewired and repositioned null models were used to assess network topology and geometry. Rewired null models are models in which structural connectivity pairs of regions are randomized while preserving the network's original degree sequence and density. Swapping of the connectivity and distance matrices was performed using the Maslov–Sneppen algorithm in the Brain Connectivity Toolbox.[66,67] The randomized matrix was inserted into the model to derive a null peak fit between atrophy patterns; this process was repeated 10 000 times to generate a distribution of null peak fits, whose average was statistically compared to the peak fit of the original model. An unbiased Monte Carlo estimate of the exact *P*-value was used to assess significance. The same steps were repeated using repositioned null models, i.e. models in which the spatial position of regions was randomized while preserving the network's original degree sequence and connection profile. A similar approach was also conducted for gene expression, where distinct null models were generated with either *SNCA* or *GBA* regional expression randomized between the 42 regions.

Data availability

The agent-based SIR model is available at https://github.com/yingqiuz/SIR_simulator. The regional values of the tissue deformation, cortical thickness and cortical surface area maps are available at https://github.com/srahayel/SIR-RBD.

Results

Demographics

Of the 443 participants, 34 did not pass DBM quality control, resulting in 409 participants (171 patients and 238 controls). There were no significant differences in age (iRBD: 67.7 ± 6.6 years; controls: 66.6 ± 7.9, $P = 0.11$) and sex (iRBD: 83% male, controls: 77% male, $P = 0.13$) between groups, but patients had higher MDS-UPDRS-III scores ($P < 0.001$) and lower MoCA scores ($P < 0.001$; Table 1). Of these 409 participants, 64 did not pass FreeSurfer quality control, resulting in 345 participants (138 iRBD patients and 207 controls) for quantifying cortical thickness and surface area differences. There were no significant differences in age (iRBD: 66.2 ± 7.6 years; controls: 67.0 ± 6.3 years; $P = 0.28$) and sex (iRBD: 81% male, controls: 77% male; $P = 0.34$) for this sample.

Patients with iRBD show brain atrophy

We investigated if this iRBD cohort showed brain atrophy compared to controls, accounting for age, sex and site. In terms of DBM, patients had decreased volume in the left middle temporal cortex, cuneus, lingual gyrus, fusiform gyrus, banks of the superior temporal sulcus and the pericalcarine area and increased volume in the insula compared to controls; in the right hemisphere, decreased volume was found in the precentral, supramarginal, superior and middle temporal, lingual and cuneus regions. However, only the left middle temporal region was significant after correction ($P_{FDR} = 0.045$; Fig. 2A and Supplementary Table 2).

For cortical thickness, patients showed significant thinning compared to controls in two clusters in the left hemisphere, namely one posterior cluster that included the posterior temporal and inferior parietal cortices and another cluster that extended from the dorsolateral prefrontal cortex to the orbitofrontal cortex, and in one cluster in the right hemisphere, which included the posterior temporal and lateral occipital cortices (Fig. 3A and Table 2). Compared to controls, patients also had significantly increased cortical surface area in the left inferior temporal cortex and sulcus that extended to the entorhinal cortex (Fig. 3B and Table 2). These findings demonstrate the presence of brain atrophy in iRBD.

Brain atrophy in iRBD is associated with motor and cognitive functioning

In iRBD patients, higher MDS-UPDRS-III scores were associated with cortical thinning in the bilateral frontal cortex and the right temporal cortex and with increased thickness in the right sensorimotor cortex (Fig. 4B and Table 2). Higher MDS-UPDRS-III scores were also associated with increased cortical surface area in the bilateral occipital cortex, the left inferior parietal cortex and the right posterior temporal cortex (Fig. 4B and Table 2). The associations with MDS-UPDRS-III scores were significantly different between iRBD patients and controls, with the correlation being stronger in patients in the bilateral sensorimotor cortex for thickness and in the frontopolar, sensorimotor, occipital, inferior parietal and lingual and fusiform cortices for surface area (Fig. 4B and Table 2). For the MoCA, lower scores were associated with cortical thinning in the bilateral insula, the right temporal cortex and the left posterior temporal cortex (Fig. 4C and Table 2). MoCA scores were not associated with cortical surface area in iRBD patients and there were no differences in correlation slopes between patients and controls.

The SIR model recreates the atrophy of iRBD

The agent-based model was then applied to simulate pathological alpha-synuclein spread and generate patterns of simulated atrophy in every region. We found that the model recreated the DBM-derived W-scored tissue deformation pattern, with the peak fit reaching $r = 0.52$ ($P < 0.0005$) when seeding from the banks of superior temporal sulcus at a connection density of 40% (Fig. 2B). The fit between atrophy patterns increased gradually with each time step to reach a peak, followed by a decline that led to the equilibrium state (Fig. 2C). At the peak, the simulated atrophy was most prominent in the pericalcarine cortex, accumbens, cuneus, substantia nigra, amygdala and the banks of the superior temporal sulcus (Fig. 2C). At later time steps, the correlation declined but simulated atrophy was seen in putamen and lingual gyrus. The model also recreated atrophy at the lower connection densities ($r = 0.44$ at 35%, $r = 0.50$ at 30%, $r = 0.36$ at 25%; Supplementary Fig. 1). The other seed regions that recreated atrophy in iRBD, although with significance over the Bonferroni-corrected threshold, were regions surrounding the banks of the superior temporal sulcus, namely the supramarginal gyrus ($r = 0.38$, $P = 0.014$), inferior parietal cortex ($r = 0.36$, $P = 0.018$), middle temporal cortex ($r = 0.330$, $P = 0.034$) and inferior temporal cortex ($r = 0.329$, $P = 0.034$).

Similarly, the model recreated the W-scored cortical atrophy pattern, derived from FreeSurfer, with the peak fit reaching $r = 0.51$ ($P = 0.0007$) for cortical thickness (Fig. 3C). However, for cortical surface area, the coefficient was slightly over the Bonferroni-corrected threshold, at $r = 0.43$ ($P = 0.006$). When assessing the fit over the 34 cortical regions only (without the subcortical measurements), only thickness was significant ($r_{thickness} = 0.48$, $P = 0.004$; $r_{area} = 0.28$, $P = 0.11$). When seeding from the postcentral gyrus, the fit for cortical thickness increased gradually and reached its peak once the system had attained the equilibrium state; at this time step, the simulated atrophy was primarily found in the frontal pole, amygdala, accumbens and entorhinal cortex (Fig. 3D). However, given the behaviour of the agent-based model to converge to an equilibrium state regardless of the seed region used, every brain region yielded a peak fit relatively close to the one generated when seeding from the postcentral

Table 1 Demographics and clinical variables of iRBD patients and controls

Variables	iRBD ($n = 171$)	Controls ($n = 238$)	P-value
Age, years	67.7 ± 6.6 (49–87)	66.6 ± 7.9 (41–88)	0.112[a]
Sex, *n* (% male)	142 (83%)	183 (77%)	0.129[b]
MDS-UPDRS-III[c]	7.4 ± 6.9 (0–34)	2.3 ± 3.7 (0–19)	<0.001[d]
UPDRS-III (Fahn and Elton)[e]	4.3 ± 3.6 (0–19)	—	—
MoCA	26.3 ± 3.1 (11–30)	27.9 ± 1.7 (20–30)	<0.001[d]

Continuous data are presented as mean ± SD (range).
[a]Student's *t*-test.
[b]Chi-squared test.
[c]Available in 123 patients and 154 controls.
[d]Mann–Whitney U-test.
[e]The Montreal cohort underwent the Fahn and Elton UPDRS-III version.

gyrus (lowest peak fit: $r = 0.502$, $P = 0.00094$). The fit was also significant at lower connection densities of the connectome ($r = 0.50$ at 35%, $r = 0.49$ at 30%, $r = 0.48$ at 25%).

To confirm that our findings were not caused by site-specific effects, the tissue deformation and cortical thickness *W*-scores were harmonized using ComBat[46,47]; the model recreated the patterns just described in a similar way ($r = 0.515$, $P = 5.69 \times 10^{-4}$ for tissue deformation, $r = 0.523$, $P = 5.50 \times 10^{-4}$ for cortical thickness). In addition, the model also recreated atrophy when using finer parcellations of 65 and 119 regions (Supplementary Fig. 2), with various spreading rates of agents (Supplementary Fig. 3), and with different weights given to misfolded alpha-synuclein accumulation versus deafferentation in the simulated atrophy ratio, with higher peak fits obtained when deafferentation was given the larger weight (Supplementary Fig. 4). Taken together, these results demonstrate that volume and cortical thickness atrophy in iRBD can be recreated by the agent-based model utilizing connectivity and gene expression.

Several genes involved in macroautophagy improve model fit

To investigate whether genes other than *GBA* may act as a clearance term that recreates atrophy in iRBD, we assessed in the model the 310 genes belonging to the Gene Ontology macroautophagy biological process gene set. Of these, 30 (10%) genes recreated atrophy at a 40% connection density when entered as the model's clearance term (Fig. 5A). *UBA5* was the gene that yielded the highest peak fit ($r = 0.572$, $P = 0.0001$), followed by *GBA* ($r = 0.517$, $P = 0.0005$), *RUBCNL* ($r = 0.497$, $P = 0.0009$), *EXOC7* ($r = 0.496$, $P = 0.0010$), *CHMP4A* ($r = 0.465$, $P = 0.0021$), *MAP1LC3B2* ($r = 0.461$, $P = 0.0024$), *ADRB2* ($r = 0.454$, $P = 0.0028$), *QSOX1* ($r = 0.430$, $P = 0.0049$), *TBC1D14* ($r = 0.427$, $P = 0.0052$) and *SNX7* ($r = 0.426$, $P = 0.0053$) (see Supplementary Table 3 for the list of genes). The average expression of these genes varied across brain regions and cell types but was generally lower than *SNCA* (Fig. 5B). This demonstrates that the agent-based SIR model can be used to generate new hypotheses regarding atrophy in the prodromal phases of synucleinopathies.

Simulated atrophy is associated with lower cognitive performance

Next, we investigated if the similarity between an individual patient's atrophy pattern and the one generated by the SIR model associated with clinical features in patients. We assessed the peak fit between the atrophy patterns for each patient and then investigated if these values correlated with the MoCA and MDS-UPDRS-III scores. This revealed that a higher similarity between the simulated atrophy and the individual patterns of atrophy was significantly associated with the MoCA ($r = -0.18$, $P = 0.046$) but not the MDS-UPDRS-III scores ($r = -0.034$, $P = 0.76$) independently from the effects of age and sex (Fig. 5C). This supports that the model recreates the atrophy associated with the development of cognitive impairment in iRBD.

Simulated atrophy outperforms gene and network metrics

To ascertain whether brain connectivity or gene expression alone could recreate the atrophy pattern as well as the full model, we also tested several network-based and other model-derived measures. For every connection density, we found that the simulated atrophy from the agent-based model always yielded the highest peak fits ($r = 0.52$, $P < 0.0005$ at 40%), followed by the number of susceptible agents ($r = 0.32$, $P = 0.039$; Fig. 5D). None of the other measures, namely the number of infected agents or those describing the network's topology, associated significantly with the observed atrophy (Fig. 5). As for gene expression, the DBM-derived tissue deformation was associated with neither *SNCA* ($r = 0.24$, $P = 0.12$) nor *GBA* ($r = 0.18$, $P = 0.24$) regional expression. This demonstrates that brain connectivity or gene expression alone cannot predict atrophy in iRBD, and that the full agent-based SIR model taking into account gene expression, connectivity and deafferentation provides the best fit to the measured deformation.

Connectivity and gene expression shape atrophy

We further investigated the importance of connectome architecture and gene expression by generating several null models. The peak fits of the SIR model were compared to the peak fits observed in null distributions derived from simulations where either gene expression or network architecture were randomly shuffled across regions. We observed that randomizing *SNCA* and *GBA* expression levels (i.e. alpha-synuclein synthesis and clearance) significantly disrupted the model fit at a 40% connection density; however, at lower connection densities, model fit was still significantly reduced by randomizing *GBA* but not *SNCA* expression (Fig. 6). The randomization of connectivity was performed using two different types of null models to assess the impact of network topology and/or geometry on alpha-synuclein spread. In both cases, randomizing the connectome's architecture disrupted the model fit (Fig. 6), indicating that both the brain's structural connectivity pattern and the physical constraints imposed on the connectome contribute to shaping atrophy. Taken together, this demonstrates that connectivity and gene expression combine to shape brain atrophy of iRBD.

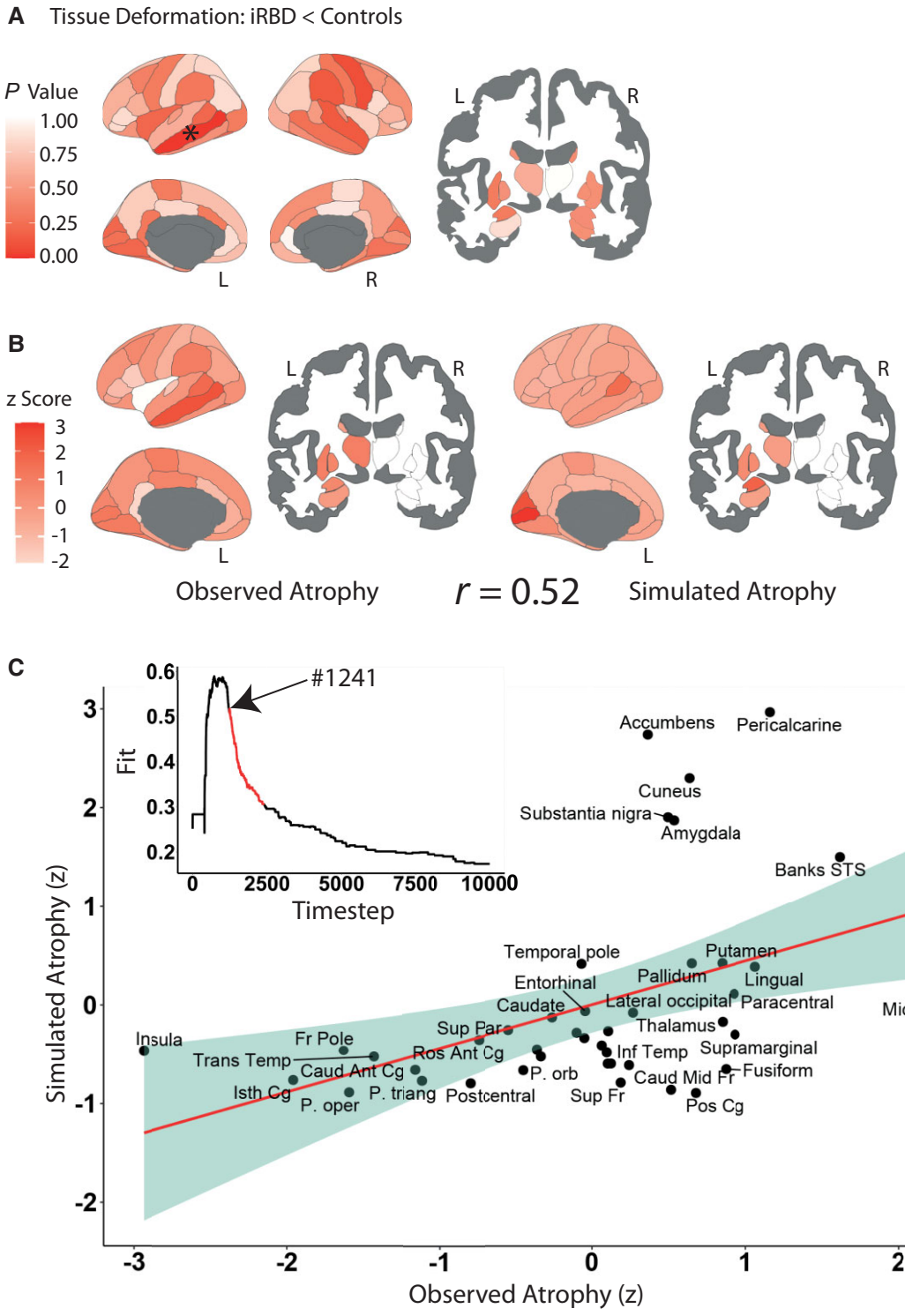

Figure 2 The model recreates the pattern of tissue deformation of iRBD. (**A**) Volume was significantly decreased in iRBD patients compared to controls. The asterisk indicates the regions that were significant when correcting for FDR. (**B**) The pattern of volume loss in iRBD (*left*) was recreated by the model (*right*). For visualization purposes, atrophy W-scores were z-scored to ease comparability of scales; positive z scores represented greater atrophy. (**C**) The subplot shows the progression of the fit between atrophy patterns until the peak at time step #1241 (arrow). The main scatterplot shows the z-scored values of observed and simulated atrophy at the peak fit for the 42 regions. Scales were adjusted such that higher scores represented greater atrophy. FDR = false discovery rate; L = left; R = right.

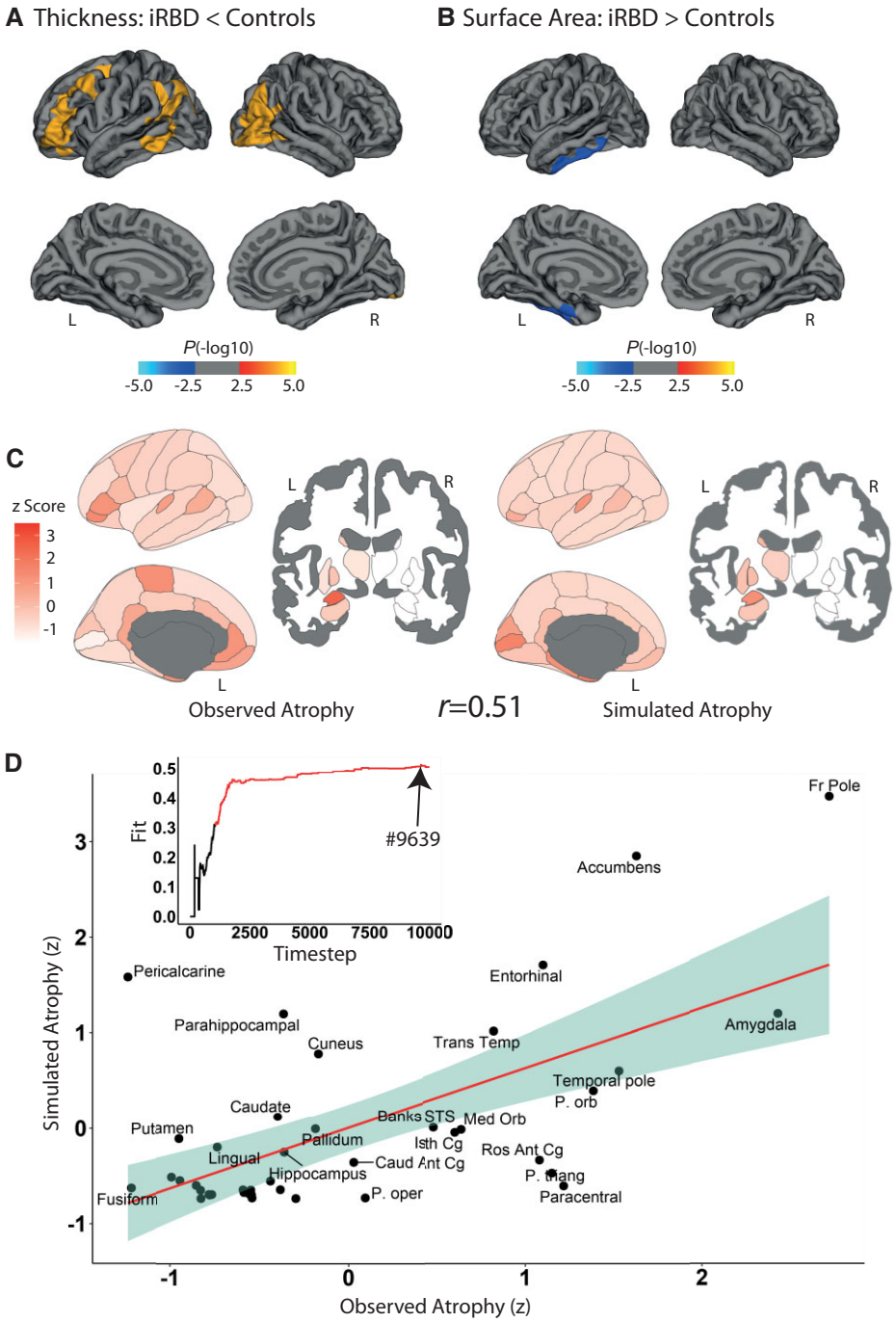

Figure 3 The model recreates the pattern of cortical thinning of iRBD. Patients with iRBD showed cortical thinning (**A**) and increased surface area (**B**) compared to controls. The colour bar indicates the statistical significance on a logarithmic scale of *P*-values (–log10), with positive values showing significant decreases in iRBD and negative values showing increases in iRBD. (**C**) The pattern of cortical thinning in iRBD (*left*) was recreated by the model (*right*). For visualization purposes, atrophy *W*-scores were z-scored to ease comparability of scales; positive z scores represented greater atrophy. (**D**) The subplot shows the progression of the fit between atrophy patterns for thickness until the peak at time step 9639 (arrow). The main scatterplot shows the z-scored values of observed and simulated atrophy at the peak fit for 41 regions (substantia nigra not included). Scales were adjusted such that higher scores represented greater atrophy. L = left; R = right.

Discussion

Isolated RBD has been associated with reductions in brain volume and cortical thickness.[7–9,68–73] Patients also present with high rates of positivity to pathologic alpha-synuclein in tissue biopsies[74–77] and CSF assays.[78] However, a mechanistic understanding of how alpha-synuclein pathology may relate to the patterns of brain atrophy in iRBD remains unknown. Here, we quantified atrophy in the largest multicentric cohort of polysomnography-confirmed iRBD patients with T_1-weighted MRI acquired to date and applied the agent-based SIR model to test whether prion-like and regional vulnerability factors recreated the atrophy in iRBD. We demonstrated

Table 2 Results of vertex-based cortical analyses between iRBD patients and controls

Cortical measure	Most affected regions	Hemisphere	Cluster size, mm^2	Number of vertices	Talairach coordinates			$-\log_{10}$ P-value
					x	y	z	
Between group comparisons								
Thickness[a]	Inferior parietal and lateral occipital	Right	5740.0	9280	41.8	−70.0	23.0	4.332
	Rostral and caudal middle frontal, superior frontal, medial orbitofrontal, pars orbitalis	Left	6470.4	10 938	−33.6	35.6	23.9	2.652
	Inferior parietal, inferior, middle, superior temporal cortex	Left	4766.7	8943	−38.2	−52.8	22.5	2.306
Surface area[b]	Inferior temporal and entorhinal	Left	2615.5	4458	−50.1	−45.3	−14.0	−2.983
MDS-UPDRS-III: Correlation analysis in iRBD								
Thickness	Inferior, middle, and superior temporal[c]	Right	3751.0	6712	54.9	−25.0	−18.1	−4.295
	Superior frontal, pars opercularis, triangularis, orbitalis, rostral and caudal middle frontal, medial and lateral orbitofrontal, precentral and postcentral[c]	Left	14557.5	26 102	−7.2	36.9	−20.6	−4.043
	Medial and lateral orbitofrontal, pars opercularis, triangularis, orbitalis[c]	Right	5389.5	8843	6.7	51.5	−17.8	−3.987
	Superior frontal, rostral and caudal middle frontal[c]	Right	5061.7	9439	9.0	38.2	28.3	−3.879
	Precentral and postcentral[d]	Right	2205.7	5010	8.3	−25.8	63.6	3.304
Surface area	Lateral occipital, fusiform[d]	Right	4636.9	6614	41.9	−69.8	5.6	4.483
	Inferior parietal, lateral occipital[d]	Left	3861.5	6219	−40.6	−71	32.6	4.059
MDS-UPDRS-III: Difference in correlation between groups								
Thickness	Precentral, postcentral, paracentral, caudal middle frontal[e]	Left	4595.2	10 528	−31.3	−19.4	54.3	−4.049
	Precentral[e]	Right	2429.5	5638	11.1	−23.6	62.0	−3.454
Surface area	Postcentral, precentral[e]	Left	2021.3	4630	−47.0	−16.2	53.2	−5.280
	Lateral occipital and fusiform[e]	Left	2116.1	2832	−34.9	−86.3	−4.9	−2.984
	Inferior parietal[e]	Left	1810.9	2952	−36.3	−74.5	31.1	−2.862
	Inferior temporal, fusiform, lingual[e]	Right	2367.9	4074	40.8	−9.9	−24.8	−2.745
	Lateral and medial orbitofrontal, superior frontal[e]	Right	2936.6	4437	14.4	30.2	−17.4	−2.316
MoCA: Correlation analysis in iRBD								
Thickness	Inferior, middle, superior temporal cortex, fusiform, lingual, entorhinal[d]	Right	7239.5	11 827	40.8	−41.8	−13.4	4.183
	Insula, pars opercularis, rostral middle frontal, lateral orbitofrontal[d]	Left	5111.6	11 651	−41.0	−0.5	14.4	4.038
	Fusiform and lingual[d]	Left	2277.5	3100	−40.6	−61.8	−7.9	3.519
	Insula, banks of STS, lateral orbitofrontal, pars opercularis[d]	Right	3774.7	9208	43.1	−18.3	18.1	2.596

STS = superior temporal sulcus. Results were corrected with Monte-Carlo simulation at $P < 0.05$ with age, sex and site entered as covariates, as well as total intracranial volume for surface area analysis. Clusters are listed by the strongest $-\log_{10}$ P-value.

[a]iRBD < Controls.

[b]iRBD > Controls.

[c]Negative association.

[d]Positive association.

[e]Stronger association in iRBD patients compared to controls.

that the computational simulation of atrophy based on connectome architecture and gene expression of *SNCA* and *GBA* did recreate the atrophy seen in iRBD patients and that a stronger resemblance between a patient's atrophy pattern and the atrophy simulated by the model was associated with lower cognitive performance in patients. This is consistent with reports that brain atrophy in iRBD associates with cognitive impairment[8] and predicts subsequent development of dementia with Lewy bodies.[9] The current study sheds light on the specific mechanisms linking pathologic alpha-synuclein, brain atrophy and cognitive impairment in iRBD.

The agent-based SIR model simulates brain atrophy due to the spread of alpha-synuclein based on brain connectivity and the expression of genes involved in alpha-synuclein synthesis and clearance.[23] This model recreates the atrophy seen in Parkinson's disease[23] and the spatiotemporal patterns of pathologic alpha-synuclein quantified in non-transgenic mice injected with preformed fibrils into either the striatum, nucleus accumbens or hippocampus.[24] In the current work, we show that the atrophy in iRBD also follows the constraints imposed by connectome architecture and the gene expression of *SNCA* and *GBA*. The impact of these factors was decisive, as demonstrated by the model's inability to recreate atrophy if either connectivity or gene expression were randomized. The influence of connectivity is in line with several studies showing that cerebral connectivity forecasts the atrophy seen in neurodegenerative diseases,[79–81] including Parkinson's disease.[22,23] The influence of *SNCA* and *GBA* gene expression also agrees with mutations in these genes being significant risk factors for Parkinson's disease and dementia with Lewy bodies.[82–84] We observed that, whereas randomizing *GBA* expression always interfered with the model's ability

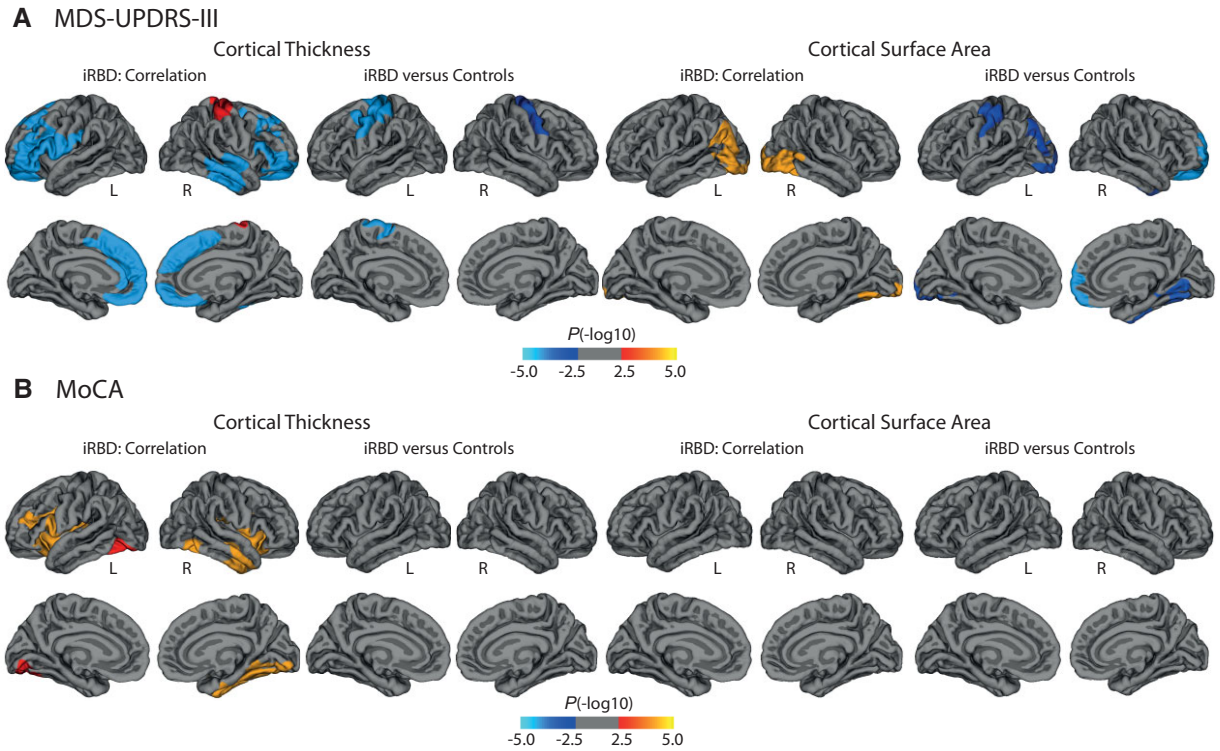

Figure 4 Correlation analyses between cortical surface and motor and cognitive variables. Results of the general linear models showing the vertices where a significant correlation was found with the MDS-UPDRS-III (**A**) and MoCA (**B**) in iRBD patients and the vertices where the slopes between the structural metric and these scores significantly differed between patients and controls. The colour bar indicates the statistical significance on a logarithmic scale of *P*-values (−log10; ±1.3 corresponding to $P < 0.05$ corrected for multiple comparisons by Monte Carlo cluster-wise simulation), with positive values showing positive associations in iRBD and negative values showing negative associations in iRBD. For comparisons of correlation, negative clusters represent stronger correlations in iRBD compared to controls. L = left; R = right.

to recreate atrophy, the randomization of *SNCA* expression only led to a disruption at the 40% connection density. *GBA* is involved in clearance of both normal and misfolded alpha-synuclein while *SNCA* only indexes synthesis of normal alpha-synuclein, possibly accounting for the former's greater influence in the model. Another possibility is that the 90 additional connections appearing in the 40% density connectome were particularly influential for *SNCA* to exert its effect on atrophy.

When testing several other genes involved in macroautophagy, *GBA* ranked second as the clearance gene that yielded the highest peak fit of the atrophy pattern in iRBD, supporting its role in the generation of brain atrophy in iRBD. It was only preceded by *UBA5*, which codes for an enzyme (ubiquitin-like modifier-activating enzyme 5, UBA5) that activates UFMylation,[85] an enzymatic cascade of protein degradation analogous to ubiquitination.[86] Instead of tagging polyubiquitin chains to worn-out proteins, UFMylation tags ubiquitin-fold modifier 1 (UFM1) to proteins to be degraded.[86] Mutations in *UBA5* have been shown to disrupt UFMylation and to cause an autosomal recessive syndrome that may include cerebellar ataxia, severe intellectual disability, microcephaly, movement disorders and early-onset epilepsy, while its knockdown in *Drosophila* and zebrafish models was shown to relate to locomotor weakness.[87,88] To date, a specific relationship between *UBA5* and dementia with Lewy bodies and Parkinson's disease has not yet been reported, but our findings show how the SIR model can generate hypotheses to be tested experimentally about new potential actors that may be involved in abnormal protein degradation.

Also, although the model recreated atrophy, the visual inspection of observed and simulated atrophy measurements at the peak fit showed some inconsistencies. For instance, while the middle temporal gyrus was the region showing the greatest tissue deformation in iRBD, the amount of simulated atrophy was modest. This could suggest that proteins other than alpha-synuclein, disease-related changes in connectivity, regional vulnerability to alpha-synuclein accumulation unaccounted for in the model and other mechanistic explanations may be involved in the observed changes in the middle temporal gyrus. Nonetheless, neighbouring regions such as the amygdala and the entorhinal cortex, which have been reported to show a high burden of Lewy pathology in various post-mortem studies,[13,89–91] were correctly found among the regions showing the highest amount of simulated atrophy.

Another novelty of this study is the comprehensive assessment of brain morphology in a large multicentric cohort of iRBD patients with polysomnography and T_1-weighted MRI acquisition. We found that iRBD patients had volume atrophy in the middle temporal gyrus and cortical thinning in the frontal, posterior temporal, occipital and inferior parietal cortices, which is in line with earlier findings in smaller iRBD cohorts.[31] In the current study, we found that the severity of parkinsonism as measured using the MDS-UPDRS-III was associated with extensive cortical thinning and with increased thickness of the sensorimotor cortex. Whereas the paracentral, sensorimotor and superior parietal areas have been associated with motor deficits in iRBD,[7,71] other regions such as the frontal and temporal cortices were not expected to be

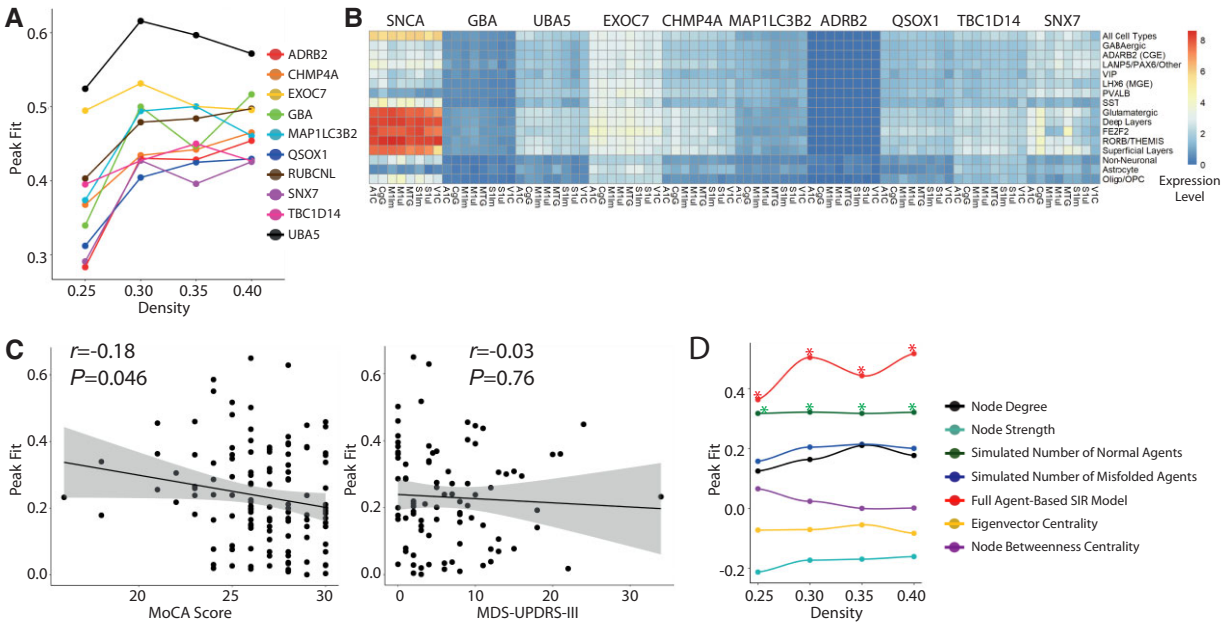

Figure 5 The SIR model allows testing hypotheses about atrophy generation and clinical features. Plot showing the macroautophagy genes that yielded the highest peak fits, as a function of connection density (**A**). Heat map showing the average expression of these genes (and *SNCA*) across brain regions and cell types based on single-nucleus RNA sequencing data from the human cortex (**B**). A stronger resemblance between an individual patient's atrophy pattern and the pattern generated by the SIR model was associated with MoCA but not MDS-UPDRS-III scores (**C**). The simulated atrophy measure generated by the full agent-based SIR model outperformed network and other model-derived measures, with asterisks representing significant correlations between atrophy patterns. A1C = primary auditory cortex; CGE = caudal ganglionic eminence; CgG = anterior cingulate gyrus; lm = lower limb; M1 = primary motor cortex; MGE = medial ganglionic eminence; MTG = middle temporal gyrus; OPC = oligodendrocyte progenitor cell; S1 = primary somatosensory cortex; ul = upper limb; V1C = primary visual cortex.

involved based on previous work. However, this frontotemporal pattern has already been documented in Parkinson's disease[92] and our findings here may represent premorbid neurodegenerative changes typical of overt Parkinson's disease uncovered thanks to our larger sample size. As for the MoCA correlates of atrophy shown here, the pattern was in line with previous observations of global cognitive performance in Parkinson's disease.[92] Notably, there was a correlation between MoCA and atrophy in the anterior insula, an area that has been shown to be particularly vulnerable in synucleinopathies affecting cognition.[93–96] Lower MoCA scores were found in iRBD patients who had a stronger resemblance of their atrophy pattern to the model simulation, supporting the idea that the constraints that shape the atrophy in the model may correspond to the ones underlying the development of atrophy in prodromal phenotypes of dementia with Lewy bodies.

This study has some limitations. First, according to the brain-first and body-first subtype hypothesis,[11] isolated RBD is thought to arise from a body-first propagation whereby pathology in the autonomic and enteric nervous system spreads to the brain, affects brainstem nuclei involved in REM sleep motor atonia[6] and then reaches other brain structures that generate parkinsonism and dementia features. However, in this study, the brainstem was not included in our analyses due to the difficulty in imaging both brain atrophy and connectivity in these structures. As soon as comprehensive atlases with gene expression and connectomic data of brainstem nuclei become available, these should be used within the SIR model to test the brain-first and body-first hypothesis. Second, the best propagator region in the SIR model is not necessarily the origin of the epidemic. The SIR model is made such that every seed region leads the model to converge to a similar equilibrium state, unless the peak fit between atrophy patterns is found during the early spreading time frame when agents are still propagating through the system; the peak fit for DBM-derived tissue deformation was found early during propagation when seeding from only a few regions, whereas the peak fit for cortical thickness was found regardless of the seed chosen. This makes the seed region analysis less relevant for understanding brain atrophy than the constraints imposed on the model, here connectomics and gene expression. Third, scans were acquired using different acquisition parameters at different sites. In the current work, site effects were regressed out from atrophy measurements during W-scoring and entered as covariates in neuroimaging analyses. The use of harmonized W-scores using a batch-correcting tool validated for neuroimaging data yielded the same results. Fourth, alpha-synuclein spread was simulated on a healthy structural connectome and transcriptome. White matter abnormalities and topological disorganization of grey matter have been reported in iRBD,[9,70,97,98] as well as a genetic makeup more complex than the sole effects of *SNCA* and *GBA*.[99] Once these changes are more thoroughly understood in iRBD, they can be implemented in the model. Fifth, the model simulates the spread based on regional gene expression and connectivity. Given that specific cell types may be vulnerable to alpha-synuclein[100] and that many transcriptomically distinct cell types have been reported in human brain tissue,[62] future studies should aim at integrating this information with whole-brain transcriptomics atlases with comprehensive cell type data once they become available.

In summary, atrophy in iRBD patients can be recreated using a combination of agent-based modelling, structural connectomics and gene expression. This further supports the theory that iRBD is a prodromal synucleinopathy. The agent-based SIR model may provide a way to test new research hypotheses for the purpose of slowing or stopping the spread of pathologic alpha-synuclein in the brain.

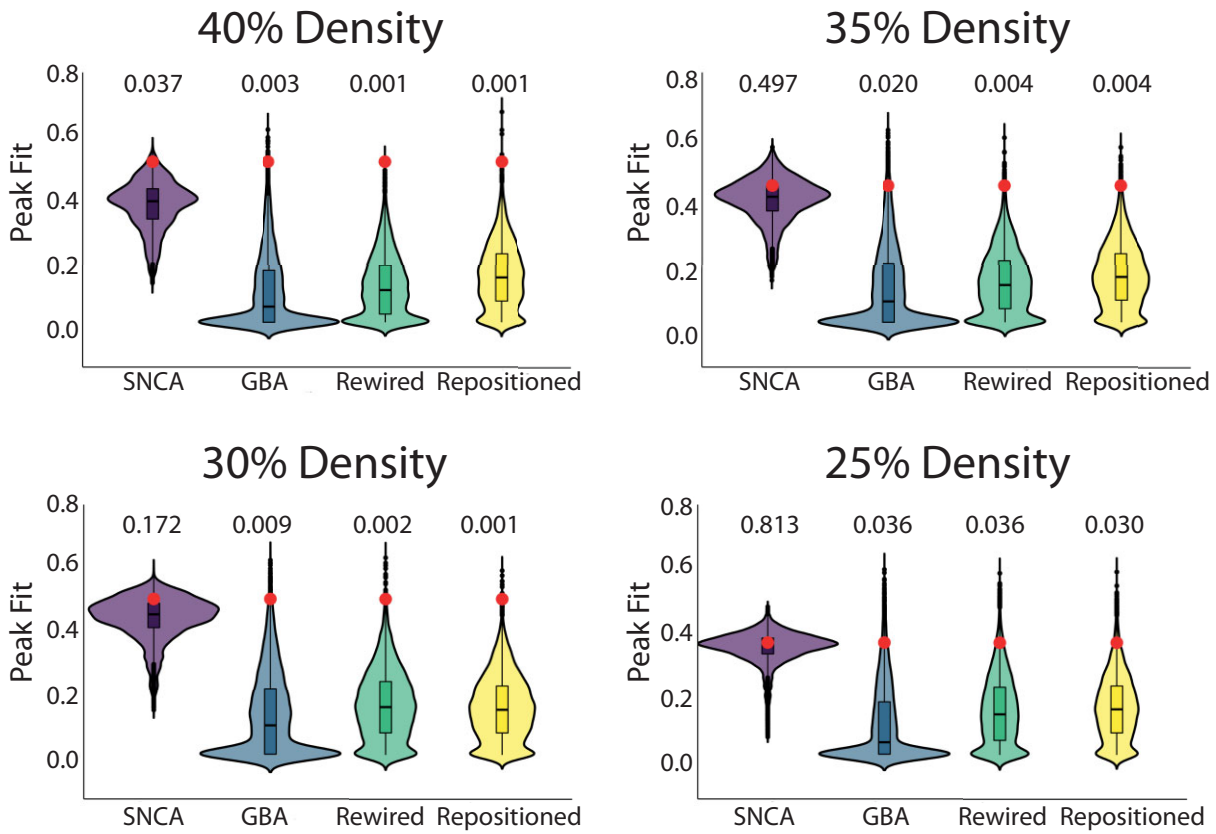

Figure 6 Gene expression and connectivity shape tissue deformation in iRBD. Violin plots comparing the original peak fits between atrophy patterns (dots) to the average peak fits derived from null models in which *SNCA* expression, *GBA* expression, network topology (rewired null models) or network geometry (repositioned null models) was randomly shuffled across regions. Unbiased Monte-Carlo estimates of the exact *P*-value were computed and reported above the plots. Comparisons with null models were performed for each connection density.

Acknowledgements

S.H. reports a scholarship from the Fonds de recherche du Québec—Santé. J-.F.G. holds a Canada Research Chair in Cognitive Decline in Pathological Aging. K.E.M. reports a scholarship from Parkinson Canada and Sydney Fellowship. Data used in this article included data from the Parkinson's Progression Markers Initiative database (https://www.ppmi-info.org), a public-private partnership, funded by the Michael J. Fox Foundation for Parkinson's Research.

Funding

The ICEBERG Study performed in Paris was funded by the Programme d'investissements d'avenir (ANR-10-IAIHU-06), the Paris Institute of Neurosciences - IHU (IAIHU-06), the Agence Nationale de la Recherche (ANR-11-INBS-0006), Électricité de France (Fondation d'Entreprise EDF), Biogen Inc., the Fondation Thérèse and René Planiol; by unrestricted support for research on Parkinson's disease from Energipole (M. Mallart) and Société Française de Médecine Esthétique (M. Legrand); and by a grant from the Institut de France to Isabelle Arnulf (for the Alice Study). The work performed in Montreal was supported by the Canadian Institutes of Health Research, the Fonds de recherche du Québec—Santé, and the W. Garfield Weston Foundation. Jean-François Gagnon reports grants from the Fonds de recherche du Québec—Santé, the Canadian Institutes of Health Research, the W. Garfield Weston Foundation, the Michael J. Fox Foundation for Parkinson's Research, and the National Institutes of Health. R.B.P. reports grants and personal fees from the Fonds de recherche du Québec—Santé, the Canadian Institutes of Health Research, The Parkinson Society of Canada, the W. Garfield Weston Foundation, the Michael J. Fox Foundation for Parkinson's Research, the R. Howard Webster Foundation, and the National Institutes of Health. This work was also funded by awards from the Canadian Institutes of Health Research Foundation Scheme and the 'Healthy Brains, Healthy Lives' program to Alain Dagher. The work performed in Sydney was supported by a Dementia Team Grant from the National Health and Medical Research Council (#1095127). S.L. is supported by a Leadership Fellowship from the National Health and Medical Research Council (#1195830). E.M. reports funding from the National Health and Medical Research Council (#2008565). The work performed in Aarhus was supported by funding from the Lundbeck Foundation, the Parkinsonforenigen (The Danish Parkinson Association), and the Jascha Foundation.

Competing interests

All authors report no competing interests related to this work.

Supplementary material

Supplementary material is available at *Brain* online.

Appendix 1

The ICEBERG Study Group

Full details are provided in the Supplementary material. Marie Vidailhet, Jean-Christophe Corvol, Isabelle Arnulf, Stéphane Lehéricy, Graziella Mangone, Sara Sambin, Jonas Ihle, Caroline Weill, David Grabli, Florence Cormier-Dequaire, Louise Laure Mariani, Bertrand Degos, Richard Levy, Fanny Pineau, Julie Socha, Eve Benchetrit, Virginie Czernecki, Marie-Alexandrine Glachant, Sophie Rivaud-Pechoux, Elodie Hainque, Smaranda Leu Semenescu, Pauline Dodet, Samir Bekadar, Alexis Brice, Suzanne Lesage, Fanny Mochel, Farid Ichou, Vincent Perlbarg, Benoit Colsch, Arthur Tenenhaus, Rahul Gaurav, Nadya Pyatigorskaya, Lydia Yahia-Cherif, Romain Valabrègue, Cécile Galléa, Marie-Odile Habert, Dijana Petrovska, Laetitia Jeancolas, Vanessa Brochard, Alizé Chalançon, Carole Dongmo-Kenfack, Christelle Laganot, Valentine Maheo.

References

1. Hogl B, Stefani A, Videnovic A. Idiopathic REM sleep behaviour disorder and neurodegeneration—An update. *Nat Rev Neurol*. 2018;14:40–55.
2. Miglis MG, Adler CH, Antelmi E, *et al*. Biomarkers of conversion to alpha-synucleinopathy in isolated rapid-eye-movement sleep behaviour disorder. *Lancet Neurol*. 2021;20:671–684.
3. Postuma RB, Iranzo A, Hu M, *et al*. Risk and predictors of dementia and parkinsonism in idiopathic REM sleep behaviour disorder: A multicentre study. *Brain*. 2019;142:744–759.
4. Galbiati A, Verga L, Giora E, Zucconi M, Ferini-Strambi L. The risk of neurodegeneration in REM sleep behavior disorder: A systematic review and meta-analysis of longitudinal studies. *Sleep Med Rev*. 2019;43:37–46.
5. Shen Y, Yu WB, Shen B, *et al*. Propagated alpha-synucleinopathy recapitulates REM sleep behaviour disorder followed by parkinsonian phenotypes in mice. *Brain*. 2020;143:3374–3392.
6. McKenna D, Peever J. Degeneration of rapid eye movement sleep circuitry underlies rapid eye movement sleep behavior disorder. *Mov Disord*. 2017;32:636–644.
7. Rahayel S, Postuma RB, Montplaisir J, *et al*. Abnormal gray matter shape. Thickness, and volume in the motor cortico-subcortical loop in idiopathic rapid eye movement sleep behavior disorder: Association with clinical and motor features. *Cereb Cortex*. 2018;28:658–671.
8. Rahayel S, Postuma RB, Montplaisir J, *et al*. Cortical and subcortical gray matter bases of cognitive deficits in REM sleep behavior disorder. *Neurology*. 2018;90:e1759–e1770.
9. Rahayel S, Postuma RB, Montplaisir J, *et al*. A prodromal brain-clinical pattern of cognition in synucleinopathies. *Ann Neurol*. 2021;89:341–357.
10. Peng C, Gathagan RJ, Lee VM. Distinct alpha-synuclein strains and implications for heterogeneity among alpha-synucleinopathies. *Neurobiol Dis*. 2018;109:209–218.
11. Horsager J, Andersen KB, Knudsen K, *et al*. Brain-first versus body-first Parkinson's disease: A multimodal imaging case-control study. *Brain*. 2020;143:3077–3088.
12. Braak H, Del Tredici K, Rub U, de Vos RA, Jansen Steur EN, Braak E. Staging of brain pathology related to sporadic Parkinson's disease. *Neurobiol Aging*. 2003;24:197–211.
13. Braak H, Ghebremedhin E, Rub U, Bratzke H, Del Tredici K. Stages in the development of Parkinson's disease-related pathology. *Cell Tissue Res*. 2004;318:121–134.
14. Rey NL, George S, Steiner JA, *et al*. Spread of aggregates after olfactory bulb injection of alpha-synuclein fibrils is associated with early neuronal loss and is reduced long term. *Acta Neuropathol*. 2018;135:65–83.
15. Rey NL, Steiner JA, Maroof N, *et al*. Widespread transneuronal propagation of alpha-synucleinopathy triggered in olfactory bulb mimics prodromal Parkinson's disease. *J Exp Med*. 2016;213:1759–1778.
16. Luk KC, Kehm V, Carroll J, *et al*. Pathological alpha-synuclein transmission initiates Parkinson-like neurodegeneration in nontransgenic mice. *Science*. 2012;338:949–953.
17. Luk KC, Kehm VM, Zhang B, O'Brien P, Trojanowski JQ, Lee VM. Intracerebral inoculation of pathological alpha-synuclein initiates a rapidly progressive neurodegenerative alpha-synucleinopathy in mice. *J Exp Med*. 2012;209:975–986.
18. Masuda-Suzukake M, Nonaka T, Hosokawa M, *et al*. Prion-like spreading of pathological alpha-synuclein in brain. *Brain*. 2013;136:1128–1138.
19. Van Den Berge N, Ferreira N, Gram H, *et al*. Evidence for bidirectional and trans-synaptic parasympathetic and sympathetic propagation of alpha-synuclein in rats. *Acta Neuropathol*. 2019;138:535–550.
20. Zeighami Y, Ulla M, Iturria-Medina Y, *et al*. Network structure of brain atrophy in *de novo* Parkinson's disease. *Elife*. 2015;4:e08440.
21. Yau Y, Zeighami Y, Baker TE, *et al*. Network connectivity determines cortical thinning in early Parkinson's disease progression. *Nat Commun*. 2018;9:12.
22. Tremblay C, Rahayel S, Vo A, *et al*. Brain atrophy progression in Parkinson's disease is shaped by connectivity and local vulnerability. *Brain Commun*. 2021;3:fcab269.
23. Zheng YQ, Zhang Y, Yau Y, *et al*. Local vulnerability and global connectivity jointly shape neurodegenerative disease propagation. *PLoS Biol*. 2019;17:e3000495.
24. Rahayel S, Misic B, Zheng YQ, *et al*. Differentially targeted seeding reveals unique pathological alpha-synuclein propagation patterns. *Brain*. 2021;145:1743–1756.
25. Marek K, Chowdhury S, Siderowf A, *et al*. The Parkinson's progression markers initiative (PPMI)—Establishing a PD biomarker cohort. *Ann Clin Transl Neurol*. 2018;5:1460–1477.
26. Postuma RB, Berg D, Stern M, *et al*. MDS Clinical diagnostic criteria for Parkinson's disease. *Mov Disord*. 2015;30:1591–1601.
27. McKeith IG, Boeve BF, Dickson DW, *et al*. Diagnosis and management of dementia with Lewy bodies: Fourth consensus report of the DLB consortium. *Neurology*. 2017;89:88–100.
28. Ashburner J, Hutton C, Frackowiak R, Johnsrude I, Price C, Friston K. Identifying global anatomical differences: Deformation-based morphometry. *Hum Brain Mapp*. 1998;6:348–357.
29. Ashburner J, Friston KJ. Unified segmentation. *Neuroimage*. 2005;26:839–851.
30. Ashburner J. A fast diffeomorphic image registration algorithm. *Neuroimage*. 2007;38:95–113.
31. Campabadal A, Segura B, Junque C, Iranzo A. Structural and functional magnetic resonance imaging in isolated REM sleep behavior disorder: A systematic review of studies using neuroimaging software. *Sleep Med Rev*. 2021;59:101495.
32. Reuter M, Schmansky NJ, Rosas HD, Fischl B. Within-subject template estimation for unbiased longitudinal image analysis. *Neuroimage*. 2012;61:1402–1418.
33. Dale AM, Fischl B, Sereno MI. Cortical surface-based analysis. I. Segmentation and surface reconstruction. *Neuroimage*. 1999;9:179–194.
34. Klapwijk ET, van de Kamp F, van der Meulen M, Peters S, Wierenga LM. Qoala-T: A supervised-learning tool for quality

control of FreeSurfer segmented MRI data. *Neuroimage*. 2019; 189:116–129.
35. Monereo-Sanchez J, de Jong JJA, Drenthen GS, *et al*. Quality control strategies for brain MRI segmentation and parcellation: Practical approaches and recommendations—Insights from the Maastricht study. *Neuroimage*. 2021;237:118174.
36. Tremblay C, Abbasi N, Zeighami Y, *et al*. Sex effects on brain structure in *de novo* Parkinson's disease: A multimodal neuroimaging study. *Brain*. 2020;143:3052–3066.
37. La Joie R, Perrotin A, Barre L, *et al*. Region-specific hierarchy between atrophy, hypometabolism, and beta-amyloid (abeta) load in Alzheimer's disease dementia. *J Neurosci*. 2012;32:16265–16273.
38. Desikan RS, Segonne F, Fischl B, *et al*. An automated labeling system for subdividing the human cerebral cortex on MRI scans into gyral based regions of interest. *Neuroimage*. 2006;31:968–980.
39. Fischl B, Salat DH, Busa E, *et al*. Whole brain segmentation: automated labeling of neuroanatomical structures in the human brain. *Neuron*. 2002;33:341–355.
40. Biondetti E, Santin MD, Valabregue R, *et al*. The spatiotemporal changes in dopamine, neuromelanin and iron characterizing Parkinson's disease. *Brain*. 2021;144:3114–3125.
41. Barber TR, Griffanti L, Bradley KM, *et al*. Nigrosome 1 imaging in REM sleep behavior disorder and its association with dopaminergic decline. *Ann Clin Transl Neurol*. 2020;7:26–35.
42. Keuken MC, Bazin PL, Crown L, *et al*. Quantifying inter-individual anatomical variability in the subcortex using 7 T structural MRI. *Neuroimage*. 2014;94:40–46.
43. Hawrylycz MJ, Lein ES, Guillozet-Bongaarts AL, *et al*. An anatomically comprehensive atlas of the adult human brain transcriptome. *Nature* 20 2012;489:391–399.
44. Yeh CH, Jones DK, Liang X, Descoteaux M, Connelly A. Mapping structural connectivity using diffusion MRI: Challenges and opportunities. *J Magn Reson Imaging*. 2021;53:1666–1682.
45. Maier-Hein KH, Neher PF, Houde JC, *et al*. The challenge of mapping the human connectome based on diffusion tractography. *Nat Commun*. 2017;8:1349.
46. Barnes J, Ridgway GR, Bartlett J, *et al*. Head size, age and gender adjustment in MRI studies: A necessary nuisance? *Neuroimage*. 2010;53:1244–1255.
47. Winkler AM, Kochunov P, Blangero J, *et al*. Cortical thickness or grey matter volume? The importance of selecting the phenotype for imaging genetics studies. *Neuroimage*. 2010;53:1135–1146.
48. Fortin JP, Cullen N, Sheline YI, *et al*. Harmonization of cortical thickness measurements across scanners and sites. *Neuroimage*. 2018;167:104–120.
49. Fortin JP, Parker D, Tunc B, *et al*. Harmonization of multi-site diffusion tensor imaging data. *Neuroimage*. 2017;161:149–170.
50. Johnson WE, Li C, Rabinovic A. Adjusting batch effects in microarray expression data using empirical Bayes methods. *Biostatistics*. 2007;8:118–127.
51. Shafiei G, Bazinet V, Dadar M, *et al*. Network structure and transcriptomic vulnerability shape atrophy in frontotemporal dementia. *Brain*. Published online 21 February 2022. doi:10.1093/brain/awac069
52. Van Essen DC, Smith SM, Barch DM, *et al*. The WU-Minn human connectome project: An overview. *Neuroimage*. 2013;80:62–79.
53. Betzel RF, Griffa A, Hagmann P, Misic B. Distance-dependent consensus thresholds for generating group-representative structural brain networks. *Netw Neurosci*. 2019;3:475–496.
54. Misic B, Betzel RF, Griffa A, *et al*. Network-based asymmetry of the human auditory system. *Cereb Cortex*. 2018;28:2655–2664.
55. Mišić B, Betzel RF, Nematzadeh A, *et al*. Cooperative and competitive spreading dynamics on the human connectome. *Neuron*. 2015;86:1518–1529.
56. Markello RD, Shafiei G, Zheng YQ, Misic B. *abagen: A toolbox for the Allen brain atlas genetics data*. Zenodo; 2020.
57. Arnatkeviciute A, Fulcher BD, Fornito A. A practical guide to linking brain-wide gene expression and neuroimaging data. *Neuroimage*. 2019;189:353–367.
58. Benjamini Y, Drai D, Elmer G, Kafkafi N, Golani I. Controlling the false discovery rate in behavior genetics research. *Behav Brain Res*. 2001;125:279–284.
59. Mowinckel AM, Vidal-Piñeiro D. Visualization of brain statistics with R Packages ggseg and ggseg3d. *Adv Methods Pract Psychol Sci*. 2020;3:466–483.
60. Subramanian A, Tamayo P, Mootha VK, *et al*. Gene set enrichment analysis: A knowledge-based approach for interpreting genome-wide expression profiles. *Proc Natl Acad Sci U S A*. 2005;102:15545–15550.
61. Senkevich K, Gan-Or Z. Autophagy lysosomal pathway dysfunction in Parkinson's disease; Evidence from human genetics. *Parkinsonism Relat Disord*. 2020;73:60–71.
62. Hodge RD, Bakken TE, Miller JA, *et al*. Conserved cell types with divergent features in human versus mouse cortex. *Nature*. 2019;573:61–68.
63. Tasic B, Yao Z, Graybuck LT, *et al*. Shared and distinct transcriptomic cell types across neocortical areas. *Nature*. 2018; 563:72–78.
64. Bakken TE, Jorstad NL, Hu Q, *et al*. Comparative cellular analysis of motor cortex in human, marmoset and mouse. *Nature*. 2021;598:111–119.
65. Bakken TE, Hodge RD, Miller JA, *et al*. Single-nucleus and single-cell transcriptomes compared in matched cortical cell types. *PLoS One*. 2018;13:e0209648.
66. Rubinov M, Sporns O. Complex network measures of brain connectivity: Uses and interpretations. *Neuroimage*. 2010;52:1059–1069.
67. Maslov S, Sneppen K. Specificity and stability in topology of protein networks. *Science*. 2002;296:910–913.
68. Rahayel S, Montplaisir J, Monchi O, *et al*. Patterns of cortical thinning in idiopathic rapid eye movement sleep behavior disorder. *Mov Disord*. 2015;30:680–687.
69. Campabadal A, Segura B, Junque C, *et al*. Cortical gray matter and hippocampal atrophy in idiopathic rapid eye movement sleep behavior disorder. *Front Neurol*. 2019;10:312.
70. Holtbernd F, Romanzetti S, Oertel WH, *et al*. Convergent patterns of structural brain changes in rapid eye movement sleep behavior disorder and Parkinson's disease on behalf of the German Rapid Eye Movement Sleep Behavior Disorder study group. *Sleep*. 2021;44:zsaa199.
71. Pereira JB, Weintraub D, Chahine L, Aarsland D, Hansson O, Westman E. Cortical thinning in patients with REM sleep behavior disorder is associated with clinical progression. *NPJ Parkinsons Dis*. 2019;5:7.
72. Scherfler C, Frauscher B, Schocke M, *et al*. White and gray matter abnormalities in idiopathic rapid eye movement sleep behavior disorder: A diffusion-tensor imaging and voxel-based morphometry study. *Ann Neurol*. 2011;69:400–407.
73. Hanyu H, Inoue Y, Sakurai H, *et al*. Voxel-based magnetic resonance imaging study of structural brain changes in patients with idiopathic REM sleep behavior disorder. *Parkinsonism Relat Disord*. 2012;18:136–139.
74. Al-Qassabi A, Tsao TS, Racolta A, *et al*. Immunohistochemical detection of synuclein pathology in skin in idiopathic rapid eye movement sleep behavior disorder and parkinsonism. *Mov Disord*. 2021;36:895–904.
75. Stefani A, Iranzo A, Holzknecht E, *et al*. Alpha-synuclein seeds in olfactory mucosa of patients with isolated REM sleep behaviour disorder. *Brain*. 2021;144:1118–1126.

76. Antelmi E, Donadio V, Incensi A, Plazzi G, Liguori R. Skin nerve phosphorylated alpha-synuclein deposits in idiopathic REM sleep behavior disorder. *Neurology*. 2017;88:2128–2131.
77. Doppler K, Jentschke HM, Schulmeyer L, *et al*. Dermal phospho-alpha-synuclein deposits confirm REM sleep behaviour disorder as prodromal Parkinson's disease. *Acta Neuropathol*. 2017;133:535–545.
78. Iranzo A, Fairfoul G, Ayudhaya ACN, *et al*. Detection of alpha-synuclein in CSF by RT-QuIC in patients with isolated rapid-eye-movement sleep behaviour disorder: A longitudinal observational study. *Lancet Neurol*. 2021;20:203–212.
79. Zhou J, Gennatas ED, Kramer JH, Miller BL, Seeley WW. Predicting regional neurodegeneration from the healthy brain functional connectome. *Neuron*. 2012;73:1216–1227.
80. Tetreault AM, Phan T, Orlando D, *et al*. Network localization of clinical, cognitive, and neuropsychiatric symptoms in Alzheimer's disease. *Brain*. 2020;143:1249–1260.
81. Brown JA, Deng J, Neuhaus J, *et al*. Patient-tailored, connectivity-based forecasts of spreading brain atrophy. *Neuron*. 2019;104:856–868.e5.
82. Krohn L, Wu RYJ, Heilbron K, *et al*. Fine-mapping of SNCA in rapid eye movement sleep behavior disorder and overt synucleinopathies. *Ann Neurol*. 2020;87:584–598.
83. Avenali M, Blandini F, Cerri S. Glucocerebrosidase defects as a Major risk factor for Parkinson's disease. *Front Aging Neurosci*. 2020;12:97.
84. Chia R, Sabir MS, Bandres-Ciga S, *et al*. Genome sequencing analysis identifies new loci associated with Lewy body dementia and provides insights into its genetic architecture. *Nat Genet*. 2021;53:294–303.
85. Komatsu M, Chiba T, Tatsumi K, *et al*. A novel protein-conjugating system for Ufm1, a ubiquitin-fold modifier. *EMBO J*. 2004;23:1977–1986.
86. Gerakis Y, Quintero M, Li H, Hetz C. The UFMylation system in proteostasis and beyond. *Trends Cell Biol*. 2019;29:974–986.
87. Duan R, Shi Y, Yu L, *et al*. UBA5 mutations cause a new form of autosomal recessive cerebellar ataxia. *PLoS One*. 2016;11:e0149039.
88. Colin E, Daniel J, Ziegler A, *et al*. Biallelic variants in UBA5 reveal that disruption of the UFM1 cascade can result in early-onset encephalopathy. *Am J Hum Genet*. 2016;99:695–703.
89. Raunio A, Myllykangas L, Kero M, Polvikoski T, Paetau A, Oinas M. Amygdala alpha-synuclein pathology in the population-based Vantaa 85+ study. *J Alzheimers Dis*. 2017;58:669–674.
90. Harding AJ, Stimson E, Henderson JM, Halliday GM. Clinical correlates of selective pathology in the amygdala of patients with Parkinson's disease. *Brain*. 2002;125:2431–2445.
91. Kovari E, Gold G, Herrmann FR, *et al*. Lewy body densities in the entorhinal and anterior cingulate cortex predict cognitive deficits in Parkinson's disease. *Acta Neuropathol*. 2003;106:83–88.
92. Wilson H, Niccolini F, Pellicano C, Politis M. Cortical thinning across Parkinson's disease stages and clinical correlates. *J Neurol Sci*. 2019;398:31–38.
93. Blanc F, Colloby SJ, Philippi N, *et al*. Cortical thickness in dementia with Lewy bodies and Alzheimer's disease: A comparison of prodromal and dementia stages. *PLoS One*. 2015;10:e0127396.
94. Roquet D, Noblet V, Anthony P, *et al*. Insular atrophy at the prodromal stage of dementia with Lewy bodies: A VBM DARTEL study. *Sci Rep*. 2017;7:9437.
95. Zhong J, Pan P, Dai Z, Shi H. Voxelwise meta-analysis of gray matter abnormalities in dementia with Lewy bodies. *Eur J Radiol*. 2014;83:1870–1874.
96. Fathy YY, Jonker AJ, Oudejans E, *et al*. Differential insular cortex subregional vulnerability to alpha-synuclein pathology in Parkinson's disease and dementia with Lewy bodies. *Neuropathol Appl Neurobiol*. 2019;45:262–277.
97. Unger MM, Belke M, Menzler K, *et al*. Diffusion tensor imaging in idiopathic REM sleep behavior disorder reveals microstructural changes in the brainstem, substantia nigra, olfactory region, and other brain regions. *Sleep*. 2010;33:767–773.
98. Park KM, Lee HJ, Lee BI, Kim SE. Alterations of the brain network in idiopathic rapid eye movement sleep behavior disorder: Structural connectivity analysis. *Sleep Breath*. 2019;23:587–593.
99. Krohn L, Heilbron K, Blauwendraat C, *et al*. Genome-wide association study of REM sleep behavior disorder identifies novel loci with distinct polygenic and brain expression effects. medRxiv, https://www.medrxiv.org/content/10.1101/2021.09.08.21254232v2, 2021.
100. Gonzalez-Rodriguez P, Zampese E, Surmeier DJ. Selective neuronal vulnerability in Parkinson's disease. *Prog Brain Res*. 2020;252:61–89.